On the performance and resonant frequency of electromagnetic induction energy harvesters

B.P. Mann [a,*], N.D. Sims [b]

[a] Department of Mechanical Engineering and Material Science, Duke University, Durham, NC 27708, USA
[b] Department of Mechanical Engineering, Sheffield University, Sheffield S1 3JD, UK

ARTICLE INFO

ABSTRACT

This paper investigates the linear response of an archetypal energy harvester that uses electromagnetic induction to convert ambient vibration into electrical energy. In contrast with most prior works, the influence of the circuit inductance is not assumed negligible. Instead, we highlight parameter regimes where the inductance can alter resonance and derive an expression for the resonant frequency.

The governing equations consider the case of a vibratory generator directly powering a resistive load. These equations are non-dimensionalized and analytical solutions are obtained for the system's response to single harmonic, periodic, and stochastic environmental excitations. The presented analytical solutions are then used to study the power delivered to an electrical load.

© 2009 Elsevier Ltd. All rights reserved.

1. Introduction

Energy harvesting devices scavenge energy from the environment. The simplest type of device uses environmental disturbances to excite an inertial generator; inertial generators contain a moving mass, sometimes called a proof mass, that is suspended in reference to the generator frame by a compliant mechanism—such as springs or magnets [1,2]. When the generator frame is accelerated, the inertial mass begins to oscillate and convert environmental disturbances into mechanical energy. Transduction methods, such as electromagnetic inductance, capacitance, or piezoelectric elements, are then used to couple the oscillator with an electrical circuit for mechanical to electrical energy transfer [3–7]. A side effect of this energy transfer is an increase in the mechanical oscillator energy dissipation. The transferred electrical energy is then used directly, as studied in the present manuscript, or stored for future applications [8].

Starting with the work of Williams et al. [9], the focus has primarily been on inertial generators with linear behavior. A primary limitation of inertial generators with linear performance is that they only perform well for a narrow band of frequencies; any variation in the excitation frequency or frequencies will greatly reduce device's ability to harvest energy. This also provides an implementation challenge, since it is typically difficult to match the linear resonance of a fabricated device to an environmental frequency [2]. Recent efforts have attempted to overcome the shortcomings of linear devices by: (1) taking advantage of nonlinear phenomena to broaden the frequency response [2,10–12]; (2) adding many oscillators with staggered resonances to broaden the systems frequency response [8,13,14]; or (3) through passive or active methods to tune the device's resonance [15]. The present article contributes to the last of these strategies by

---

* Corresponding author.
  E-mail address: brian.mann@duke.edu (B.P. Mann).

providing an exact expression for the harvester's resonance in terms of the physical parameters for the inertial generator and accompanying electrical circuit.

The objective of this paper is to provide analytical solutions for the linear response of an archetypal harvester. More specifically, we investigate analytical solutions for devices that use electromagnetic induction to transfer energy between the mechanical and electrical domains. In contrast with several recent works [2,3,16–19], the present study does not neglect the influence of the circuit inductance. Thus the presented closed-form solutions can be applied to elucidate the influence of additional design choices on device performance. Another difference in the present work is that analytical solutions were obtained for several types of ambient excitation (i.e. single-harmonic, periodic, and narrow-band white noise excitations). In contrast, most prior works only consider single-harmonic excitation [8,20–23].

The content of this paper is organized as follows. The next section derives the governing equations for an archetypal harvester that uses electromagnetic induction. The governing equations have been non-dimensionalized and analytical solutions were obtained for single-harmonic, periodic, and stochastic environmental excitations. The analytical solutions were then used to study the power delivered to an electrical load before discussing general conclusions in the final section of the paper.

2. Energy harvester model

This section describes a model for the base excitation of an inertial generator that converts mechanical energy into electrical energy via electromagnetic inductance. The section is organized into a presentation of the relationships governing the energy conversion process and a formulation of the non-dimensionalized governing equations. Although an archetypal electromagnetic harvester is considered, for the case of directly powering an electrical load [9,16], the governing equations are presented for completeness.

2.1. Electromechanical coupling and energy conversion

This section describes the relationships governing the energy flow from the mechanical system to the electrical circuit (see Fig. 1). To describe the motion of the system, two reference frames were applied. The first reference frame, designated as $\hat{z}$, tracks the housing translation; the second reference frame, designated as $\hat{x}$, is used to track the motion of the magnet. Using $\hat{y} = \hat{x} - \hat{z}$ as the relative displacement between the magnet and coil, the electromechanical coupling can be written in terms of the instantaneous power

$$F_e \frac{\mathrm{d}\hat{y}}{\mathrm{d}t} = iV, \tag{1}$$

where F_e is the electrical damping force, V is the induced voltage across the coil, and i is the current in the electrical circuit of Fig. 1 b. The magnitude of the voltage induced across the coil, as described by Faraday's law of induction, is equal to the time rate of change in the magnetic flux

$$V = \frac{\mathrm{d}\Phi}{\mathrm{d}t} = \frac{\mathrm{d}\Phi}{\mathrm{d}\hat{y}} \frac{\mathrm{d}\hat{y}}{\mathrm{d}t}, \tag{2}$$

where Φ is the magnetic flux. Since Φ is a function of the spatial magnetic field (typically defined as B), the coil geometry, number of windings, construction, and the coil location within the magnetic field, we have chosen to omit a specific
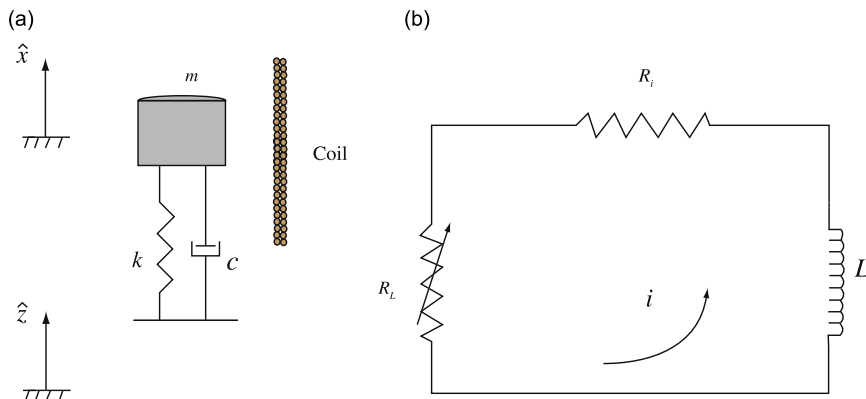

Fig. 1. Schematic diagram of an inertial energy generator that uses induction to transfer the mechanical energy of an oscillating magnet into electrical energy is shown in (a). The schematic of graph (b) shows the accompanying electrical circuit that uses the electrical energy.

expression thereby keeping the analysis that follows general. While Eq. (2) gives the voltage drop across the coil, substituting Eq. (2) into Eq. (1) gives an equation for the force that opposes the motion of the oscillating magnet

$$F_e = i\frac{\mathrm{d}\Phi}{\mathrm{d}\hat{y}}. \tag{3}$$

While the flux gradient is generally a function of space, we have assumed it to be constant over the range of interest—thus keeping the governing equations linear. Before implementing these expressions in the governing equations, we note that $\mathrm{d}\Phi/\mathrm{d}\hat{y}$ provides the electromechanical coupling between the mechanical and electrical system.

2.2. Harvester model

An equation for the electrical circuit was obtained by applying Kirchoff's voltage law to the electrical circuit of Fig. 1 b,

$$L\frac{\mathrm{d}i}{\mathrm{d}t} + i(R_L + R_i) = \frac{\mathrm{d}\Phi}{\mathrm{d}\hat{y}}\frac{\mathrm{d}\hat{y}}{\mathrm{d}t}, \tag{4}$$

where L is the inductance, R_i is the internal resistance of the coil and R_L is the resistance of the external load. The equation for the mechanical system was obtained from a summation of forces in the vertical direction

$$m\frac{\mathrm{d}^2\hat{y}}{\mathrm{d}t^2} + c\frac{\mathrm{d}\hat{y}}{\mathrm{d}t} + k\hat{y} + i\frac{\mathrm{d}\Phi}{\mathrm{d}\hat{y}} = -m\frac{\mathrm{d}^2\hat{z}}{\mathrm{d}t^2}, \tag{5}$$

where m is the inertial mass, k is the spring stiffness, c is a constant used to described the mechanical damping and $\mathrm{d}^2\hat{z}/\mathrm{d}t^2$ is the base acceleration. For the sake of analytical convenience, Eqs. (4) and (5) were non-dimensionalized using the following substitutions:

$$2\zeta\omega = \frac{c}{m}, \quad \omega^2 = \frac{k}{m}, \quad \tau = \omega t, \quad y = \frac{\hat{y}}{l}, \quad z = \frac{\hat{z}}{l} \quad \text{and} \quad I = \frac{i}{i_m}, \tag{6}$$

where ζ is the damping ratio, ω is the natural frequency, τ is dimensionless time, l is the maximum displacement allowed by physical constraints, and i_m is a threshold or reference current. The resulting non-dimensional equations are

$$\dot{I} + \alpha I = \beta\dot{y}, \tag{7a}$$

$$\ddot{y} + 2\zeta\dot{y} + y + \gamma I = -\ddot{z}, \tag{7b}$$

where a dot denotes a derivative with respect to dimensionless time and the dimensionless constants,

$$\alpha = \frac{R_L + R_i}{\omega L}, \quad \beta = \frac{1}{i_m L}\frac{\mathrm{d}\Phi}{\mathrm{d}y} \quad \text{and} \quad \gamma = \frac{i_m}{m\omega^2 l^2}\frac{\mathrm{d}\Phi}{\mathrm{d}y} \tag{8}$$

have been defined in terms of the original physical parameters. For the purposes of clarifying the results that follow, we note that both α and β contain L. This means that multiplying α and β by a constant is identical to changing in L while holding all other parameters constant. Similarly, a change in R_L would only alter α, again assuming all other parameters remained unchanged.

3. Response to various types of ambient vibration

This section investigates the response behavior of the electromagnetic harvester model to different types of ambient vibration. Investigations first consider a simple input—in the form of harmonic base excitation—before investigating more complex excitations. The single-harmonic results are followed by the investigation of periodic-base excitation and predictions for narrow-band white noise.

3.1. Single-frequency base excitation

This section derives the harvester's response when subjected to single-frequency base excitation. A base excitation was assumed in the form, $\hat{A}\cos\Omega t$, where Ω represents the excitation frequency and $\hat{A}$ the acceleration amplitude. A dimensionless form for the base excitation, $\ddot{z} = A\cos\eta\tau$, was obtained by defining $\eta = \Omega/\omega$ and $A = \hat{A}/l\omega^2$. Inserting this excitation into Eq. (7b) gives

$$\dot{I} + \alpha I = \beta\dot{y}, \tag{9a}$$

$$\ddot{y} + 2\zeta\dot{y} + y + \gamma I = A\cos\eta\tau. \tag{9b}$$

The steady-state response of the system was determined by applying the method of undetermined coefficients. The assumed form for the steady-state response is

$$y(\tau) = a\cos(\eta\tau + \phi) = \tfrac{1}{2}a(e^{j(\eta\tau + \phi)} + e^{-j(\eta\tau + \phi)}), \tag{10a}$$

$$I(\tau) = b\cos(\eta\tau + \psi) = \tfrac{1}{2}b(e^{j(\eta\tau + \psi)} + e^{-j(\eta\tau + \psi)}), \tag{10b}$$

where $j = \sqrt{-1}$, a is the response amplitude of the mass and ϕ is the phase response relative to the input excitation; the parameters b and ψ represent the response amplitude and phase of the electrical current. The following two equations were obtained after substituting Eqs. (10a) and (10b) into Eqs. (9a) and (9b) and collecting the coefficients of $e^{j\eta\tau}$,

$$(j\eta + \alpha)b = j\beta\eta a e^{j(\phi - \psi)}, \tag{11a}$$

$$(1 - \eta^2 + 2j\zeta\eta)a e^{j(\phi - \psi)} + \gamma b = A e^{-j\psi}. \tag{11b}$$

The second of these two equations was separated into real and imaginary terms to obtain

$$A\cos\psi = (1 - \eta^2)a\cos(\phi - \psi) - (2\zeta\eta)a\sin(\phi - \psi) + \gamma b, \tag{12a}$$

$$-A\sin\psi = (1 - \eta^2)a\sin(\phi - \psi) + (2\zeta\eta)a\cos(\phi - \psi). \tag{12b}$$

Eq. (11a) was also separated into real and imaginary terms to obtain Eqs. (13a) and (13b). Squaring and adding these two equations gives the relationship of Eq. (13c),

$$a\sin(\phi - \psi) = -\frac{b\alpha}{\beta\eta}, \tag{13a}$$

$$a\cos(\phi - \psi) = \frac{b}{\beta}, \tag{13b}$$

$$b = a\frac{\beta\eta}{\sqrt{\alpha^2 + \eta^2}}. \tag{13c}$$

The steady-state amplitude of the dimensionless electrical circuit was found by substituting Eqs. (13a)–(13c) into Eqs. (12a) and (12b). After squaring and summing the resultant equations, the following solution was obtained for the response of the electrical circuit

$$b = \frac{A\beta\eta}{[(\alpha^2 + \eta^2)((1 - \eta^2)^2 + (2\zeta\eta)^2) + 2\beta\gamma\eta^2(1 + 2\alpha\zeta - \eta^2) + (\gamma\beta\eta)^2]^{1/2}}. \tag{14}$$

The response amplitude of the mass was obtained by combining Eqs. (13c) and (14) to formulate the following expression:

$$a = \frac{A\sqrt{\alpha^2 + \eta^2}}{[(\alpha^2 + \eta^2)((1 - \eta^2)^2 + (2\zeta\eta)^2) + 2\beta\gamma\eta^2(1 + 2\alpha\zeta - \eta^2) + (\gamma\beta\eta)^2]^{1/2}}. \tag{15}$$

The above result is rather instructive since removing the coupling between the mechanical and electrical systems, by setting $\beta = \gamma = 0$, returns the exact response for the linear harmonic oscillator.

The steady-state phase response can also be determined from the results of this section. Specifically, Eqs. (12a)–(13c) were used to determine the phase response of the electrical circuit,

$$\psi = \tan^{-1}\left(\frac{2\zeta + \alpha(\eta^2 - 1)}{\eta(\eta^2 - 1 - 2\alpha\zeta - \gamma\beta)}\right), \tag{16}$$

along with the corresponding phase response for the oscillating magnet

$$\phi = \psi - \sin^{-1}\left(\frac{\alpha}{\sqrt{\alpha^2 + \eta^2}}\right). \tag{17}$$

The analytical solutions of Eqs. (14)–(17) were used to study the response behavior for several parameter combinations. The primary observations from our studies have been summarized in the graphs of Figs. 2–4. Focusing on the reference case of Fig. 2, the predictions show prototypical behavior for the response amplitudes and phase. More specifically, the peak response or resonance occurs near $\eta = 1$ for both the mass and circuit—a result that is in agreement with the findings of several prior works [8,9,22]. The first contrasting case is shown in Fig. 3; notice that the resonance for the mass is no longer near $\eta = 1$, although the maximum current still occurs near $\eta = 1$. These counter-intuitive analytical predictions, results that mimic a resistive load change from the results of Fig. 2, were confirmed with simulation (see markers from simulated results in Fig. 3). Perhaps the most interesting case is shown in Fig. 4, where the maximum current is also shown to occur far away from $\eta = 1$. This response was obtained for the same parameters as those of Fig. 3, with the exception of multiplying α and β by a constant to mimic a different inductance.
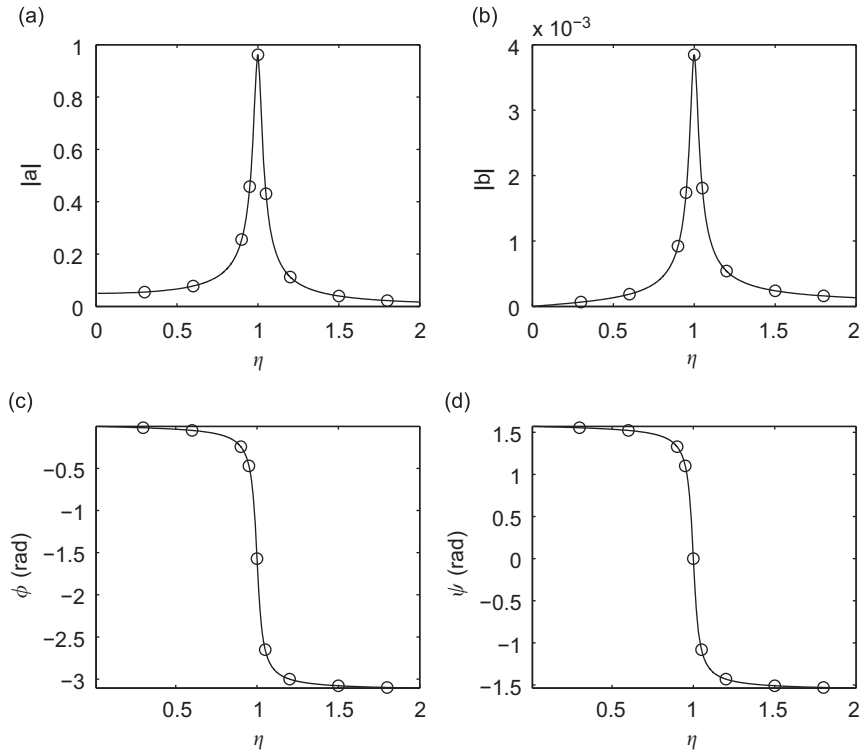
Fig. 2. Response amplitude and phase relationships for the mass (graphs (a) and (c)) and the electric circuit (graphs (b) and (d)) when excited by a single harmonic. A solid line represents analytical predictions and the marker ∘ denotes a result from simulation. The following parameters were used to generate these graphs $\alpha = 2500$, $\beta = 10$, $\zeta = 0.01$, $\gamma = 8$, and $A = \frac{1}{20}$.
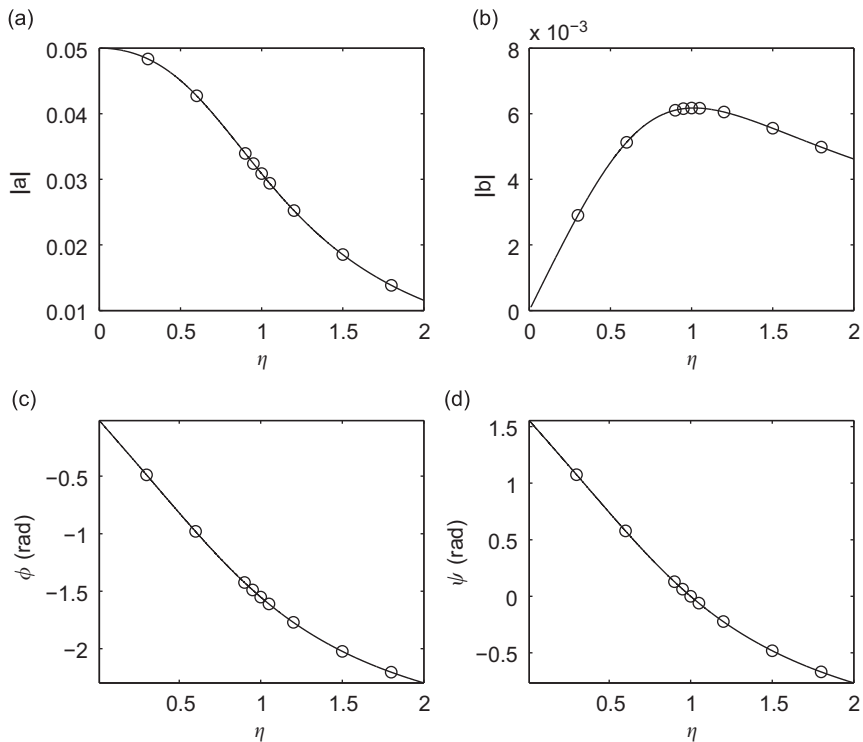

Fig. 3. Response amplitude and phase relationships for the mass (graphs (a) and (c)) and the electric circuit (graphs (b) and (d)) when excited by a single harmonic. A solid line represents analytical predictions and the marker ∘ denotes a result from simulation. The following parameters were used to generate these graphs $\alpha = 50$, $\beta = 10$, $\zeta = 0.01$, $\gamma = 8$, and $A = \frac{1}{20}$.
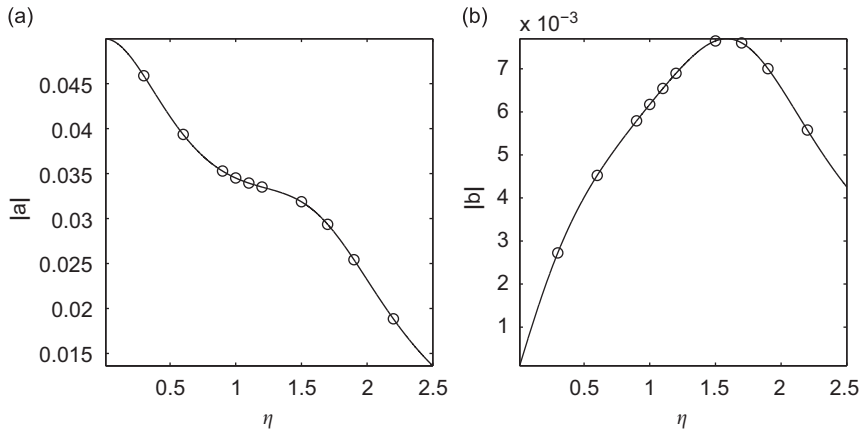
Fig. 4. Response amplitude for the mass (graph (a)) and the electric circuit (graph (b)) when excited by a single harmonic. A solid line represents analytical predictions and the marker ∘ denotes a result from simulation. The following parameters were used to generate these graphs $\alpha = 2$, $\beta = 0.4$, $\zeta = 0.01$, $\gamma = 8$, and $A = \frac{1}{20}$.
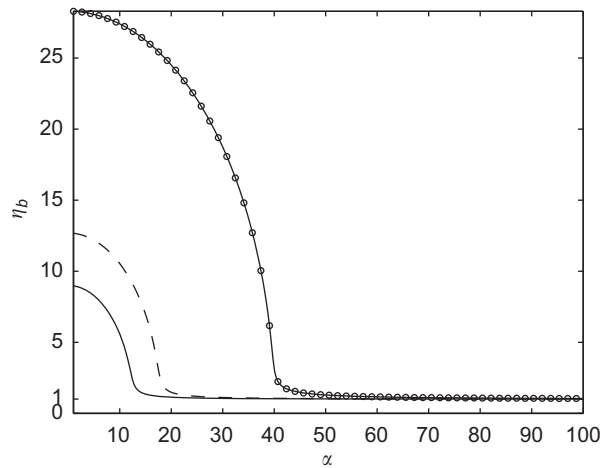

Fig. 5. Dimensionless resonance frequency plotted as a function of α. Each curve represents the following value of β: solid line $\beta = 10$, dashed line $\beta = 20$, and solid line with ∘ markers for $\beta = 100$. The following additional parameters were used: $\zeta = 0.01$ and $\gamma = 8$.

The counter-intuitive results of Figs. 2–4 can be explained by developing an analytical expression for resonance. For instance, the extrema of Eq. (14) are found from $\mathrm{d}b/\mathrm{d}\eta = 0$, which gives the following polynomial expression:

$$\eta_b^6 + \left(\frac{\alpha^2}{2} + 2\zeta^2 - \beta\gamma - 1 \right) \eta_b^4 - \frac{\alpha^2}{2} = 0, \tag{18}$$

where η_b is the dimensionless resonant frequency. While Eq. (18) predicts the peak current in Figs. 2–4, the η_b trends of Fig. 5 provide additional insight. In particular, this graph shows three η_b curves, where β was held constant and α varied, that indicate η_b is very sensitive to β for small values of α; we note that varying only alpha means that the inductance was held constant. If both alpha and beta are multiplied by a constant, which mimics an inductance change, the result in Fig. 5 is a jump to a different curve. This essentially extends the range where the resonance frequency is influenced by varying either inductance or resistance. For sufficiently large values of α, all the curves coalesce and η_b is nearly independent of changes in either α or β; this illustrates that inductance changes have very little influence within this region.

To summarize, the analytical solutions obtained in this section show responses that replicate the intuitive results of prior work, i.e. the resonance for the oscillator displacement and current may occur near $\eta = 1$. However, multiple counter-intuitive cases were presented for other parameter regimes where the inductance was shown to significantly alter the response behavior. For all of the cases shown, we have overlaid numerical simulation results to provide an external check and illustrate the strong agreement with the closed form solutions. Furthermore, we have shown regions where the resonance is sharply dependent upon the parameters of the electrical circuit and regions where the resonance is nearly independent of parameters in the electrical circuit. Our results also indicate that changes in the inductance, mimicked through simultaneous α and β changes, can either shrink or expand the region where resonance tuning can be achieved.

3.2. Periodic base excitation

The response of an energy harvester is intimately coupled to excitation provided by the environment. Thus it is relevant to consider the harvester's response to various types of ambient vibration; accordingly, this section derives the harvester response to an arbitrary-periodic excitation. For these cases, the response behavior can be generically determined when the excitation is written as a Fourier series. This provides the motivation for the current section where the harvester's response was determined as a function of the input Fourier series coefficients.

A periodic acceleration with zero mean was assumed for the base excitation; this can be expressed as a summation of harmonics, $\sum_{p=1}^{\infty} \hat{A}_p \cos p(\Omega t + \lambda)$, of acceleration amplitude $\hat{A}_p$ shifted by λ. Using the following two relationships, $\eta = \Omega/\omega$ and $A_p = \hat{A}_p/l\omega^2$, the dimensional excitation was converted into a dimensionless excitation of the form $\sum_{p=1}^{\infty} A_p \cos p(\eta\tau + \lambda)$. Inserting the periodic excitation into the governing equations gives

$$\dot{I} + \alpha I = \beta\dot{y}, \tag{19a}$$

$$\ddot{y} + 2\zeta\dot{y} + y + \gamma I = \sum_{p=1}^{\infty} A_p \cos p(\eta\tau + \lambda). \tag{19b}$$

The steady-state solution takes the following form:

$$y(\tau) = \frac{1}{2} \sum_{p=1}^{\infty} a_p (e^{jp(\eta\tau + \phi)} + e^{-jp(\eta\tau + \phi)}), \tag{20a}$$

$$I(\tau) = \frac{1}{2} \sum_{p=1}^{\infty} b_p (e^{jp(\eta\tau + \psi)} + e^{-jp(\eta\tau + \psi)}). \tag{20b}$$

After substituting Eqs. (20a) and (20b) into Eqs. (19a) and (19b) and collecting the coefficients of $e^{jp\eta\tau}$, the following two equations were obtained:

$$(j\kappa + \alpha)b_p = j\beta\kappa a_p e^{jp(\phi - \psi)}, \tag{21a}$$

$$(1 - \kappa^2 + 2j\kappa\zeta)a_p e^{jp(\phi - \psi)} + \gamma b_p = A_p e^{-jp(\lambda - \psi)}, \tag{21b}$$

where the following substitution, $\kappa = p\eta$, has been applied. Following the solution procedure outlined in Section 3.1, Eqs. (21a) and (21b) can be separated into real and imaginary terms to determine the response of the system. The following solution was obtained for the p th harmonic of the dimensionless electrical circuit

$$b_p = \frac{A_p \kappa\beta}{[(\alpha^2 + \kappa^2)((1 - \kappa^2)^2 + (2\zeta\kappa)^2) + 2\gamma\beta\kappa^2(1 + 2\alpha\zeta - \kappa^2) + (\kappa\gamma\beta)^2]^{1/2}}. \tag{22}$$

The corresponding response of the mass to the p th harmonic was determined to be

$$a_p = \frac{A_p \sqrt{\alpha^2 + \kappa^2}}{[(\alpha^2 + \kappa^2)((1 - \kappa^2)^2 + (2\zeta\kappa)^2) + 2\gamma\beta\kappa^2(1 + 2\alpha\zeta - \kappa^2) + (\kappa\gamma\beta)^2]^{1/2}}. \tag{23}$$

The phase relationships for the harvester's response were found to be

$$\psi = \lambda + \tan^{-1}\left(\frac{2\zeta + \alpha(\eta^2 - 1)}{\eta(\eta^2 - 1 - 2\alpha\zeta - \gamma\beta)}\right), \tag{24a}$$

$$\phi = \psi - \sin^{-1}\left(\frac{\alpha}{\sqrt{\alpha^2 + \eta^2}}\right). \tag{24b}$$

Example response predictions were investigated by approximating the input excitation of a square wave with a Fourier series. If we denote the square wave as $f(\tau)$, the following equations can be used to obtain the Fourier series terms A_p and λ:

$$\lambda = \tan^{-1}\left(\frac{\int_0^T f(\tau)\sin(\eta\tau)\,d\tau}{\int_0^T f(\tau)\cos(\eta\tau)\,d\tau}\right), \tag{25a}$$

$$A_p = \frac{2}{T}\int_0^T f(\tau)\cos p(\eta\tau + \lambda)\,d\tau, \tag{25b}$$

where $T = 2\pi/\eta$. These terms were inserted into $A_p \cos p(\eta\tau + \lambda)$ to approximate the actual excitation function $f(\tau)$. In our studies, the first 20 terms of the Fourier series were used to approximate the square wave function shown in Fig. 6a. Graphs (b) and (c) of Fig. 6 also show one period of the response behavior for both the mass and electrical circuit. The spectral amplitudes for the input excitation and responses of the system have been summarized in Fig. 7. One can see that the largest spectral amplitude occurs near resonance for the electrical circuit, but relatively large spectral amplitudes occur
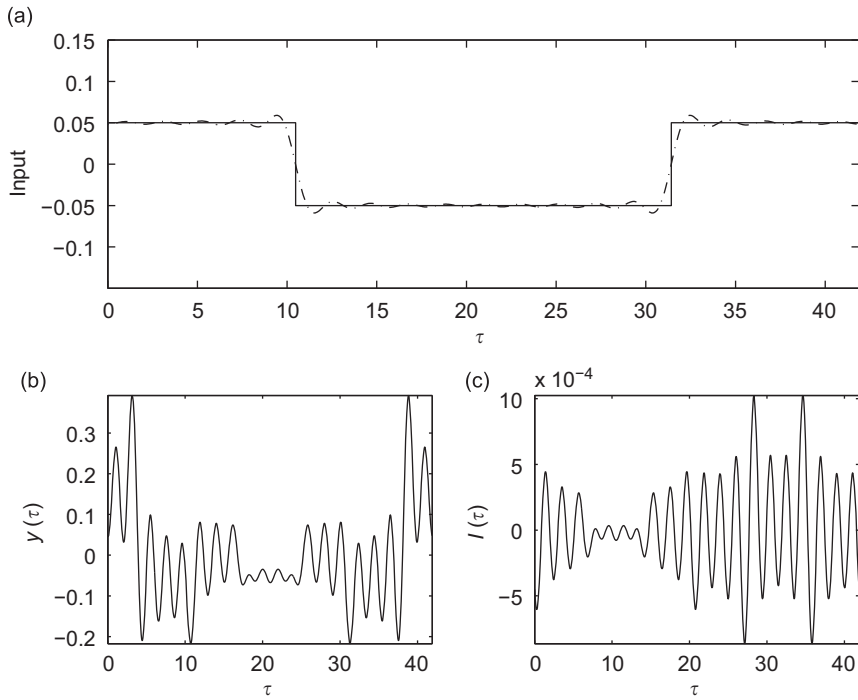
Fig. 6. Square wave excitation (solid line), with alternating amplitudes of $\pm\frac{1}{20}$, is plotted against the Fourier series approximation (dashed line) for the first 20 harmonics (graph (a)). Graphs (b) and (c) give one period, $T = 2\pi/\eta$, of the time series for $y(\tau)$ and $I(\tau)$, respectively. The following parameters were used to generate this graph $\alpha = 2500$, $\beta = 10$, $\zeta = 0.01$, $\gamma = 8$, and $\eta = 0.15$.
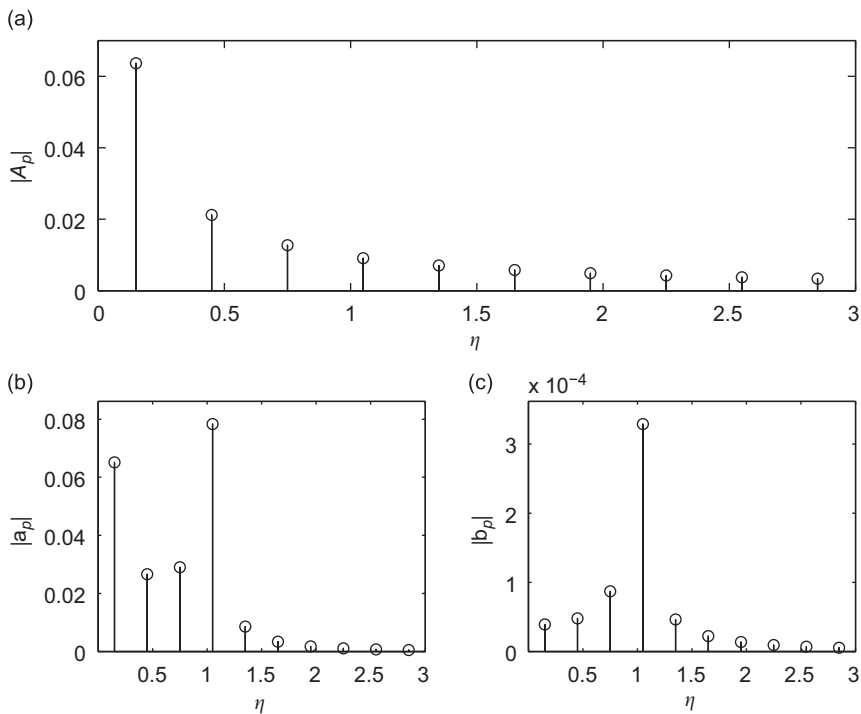

Fig. 7. Graph (a) shows the spectral amplitudes of the first 20 harmonics with a solid line and the non-zero peaks with a ∘. The response amplitudes for the mass and electrical circuit use the same markings for graphs (b) and (c), respectively. These results used the square wave from Fig. 6 a and the following parameters: $\alpha = 2500$, $\beta = 10$, $\zeta = 0.01$, $\gamma = 8$, and $\eta = 0.15$.

at both the excitation frequency and near resonance for the mass. One general observation that can be made from our studies was that more harmonics were required for η values less than one.

3.3. Response to narrow-band white noise

The response of the system to random environmental disturbances will be investigated in this section. In particular, we investigated the system's response to narrow-band white noise. Following Ref. [24], we have approximated this type of excitation with a summation of harmonic terms containing random frequency and phase components. The governing equations are

$$\dot{I} + \alpha I = \beta \dot{y}, \tag{26a}$$

$$\ddot{y} + 2\zeta\dot{y} + y + \gamma I = \Gamma \sum_{r=1}^{\infty} \cos(\eta_r\tau + \lambda_r), \tag{26b}$$

where Γ is a scaling constant, λ_r is a random phase, and η_r is a random dimensionless frequency ratio chosen on the interval between a minimum and maximum frequency ratio. Following the previously discussed solution procedures, we assumed a steady-state solution in the following form:

$$y(\tau) = \frac{1}{2}\sum_{r=1}^{\infty} a_r(e^{j(\eta_r\tau+\phi_r)} + e^{-j(\eta_r\tau+\phi_r)}), \tag{27a}$$

$$I(\tau) = \frac{1}{2}\sum_{r=1}^{\infty} b_r(e^{j(\eta_r\tau+\psi_r)} + e^{-j(\eta_r\tau+\psi_r)}). \tag{27b}$$

This results in the following response amplitude and phase relationships for the r th frequency

$$a_r = \frac{\Gamma\sqrt{\alpha^2+\eta_r^2}}{[(\alpha^2+\eta_r^2)((1-\eta_r^2)^2+(2\zeta\eta_r)^2)+2\beta\gamma\eta_r^2(1+2\alpha\zeta-\eta_r^2)+(\gamma\beta\eta_r)^2]^{1/2}}, \tag{28a}$$

$$b_r = \frac{\beta\Gamma\eta_r}{[(\alpha^2+\eta_r^2)((1-\eta_r^2)^2+(2\zeta\eta_r)^2)+2\beta\gamma\eta_r^2(1+2\alpha\zeta-\eta_r^2)+(\gamma\beta\eta_r)^2]^{1/2}}, \tag{28b}$$

and

$$\psi_r = \lambda_r + \tan^{-1}\left(\frac{2\zeta+\alpha(\eta_r^2-1)}{\eta_r(\eta_r^2-1-2\alpha\zeta-\gamma\beta)}\right), \tag{29a}$$

$$\phi_r = \psi_r - \sin^{-1}\left(\frac{\alpha}{\sqrt{\alpha^2+\eta_r^2}}\right). \tag{29b}$$

Since the form of this solution was already confirmed for the case of a single harmonic, we have chosen to omit plots of the time series.

4. Power delivered to an electrical load

This section determines relationships for the power delivered to an electrical load. In the analyses that follow, the material has been divided into separate sections that differentiate between the types of excitation studied in Section 3.

4.1. Single-frequency case

This section investigates the power delivered to an electrical load for single-harmonic excitation. Results are presented in terms of a dimensionless power ratio that accounts for the characteristics of the electrical load. More specifically, we have assumed a power threshold, $\hat{P}_m$, and voltage, v_m; this allows the reference current, a parameter that was previously used in the non-dimensionalization, to be evaluated from $i_m = \hat{P}_m/v_m$. If the threshold voltage is expressed as $v_m = i_m R_i$, the following expression is obtained for the threshold power $\hat{P}_m = i_m^2 R_i$. The instantaneous power delivered to the electrical load, $\hat{P} = i^2 R_L$, is then divided by $\hat{P}_m$ to determine the ratio of the instantaneous to the threshold power. Substituting the previously defined relationships for $i = i_m I$, $\tau = \omega t$, and $\eta = \Omega/\omega$ into this ratio gives

$$P(\tau) = \frac{i_m^2 I^2}{\hat{P}_m}R_L = \frac{R_L}{2R_i}b^2(1+\cos 2(\eta\tau+\psi)). \tag{30}$$

Although an instantaneous value is sometimes of interest, the average power is often a more meaningful quantity. The ratio of the average power to the threshold power was obtained by integrating $P(\tau)$ over a single period,

$$P_a = \frac{1}{T} \int_0^T P(\tau)\,d\tau = \frac{R_L}{2R_i} b^2,$$

(31)

where $T = 2\pi/\eta$.

A representative result, one that matches the findings from prior works, where the maximum power depends only on the resistive load, is shown in Fig. 8. Taking the physical parameters of the solid-line curve as a reference, a change in the inductance parameter was implemented by multiplying the dimensionless parameters α and β by a constant, to generate the dotted-line results of Fig. 8 a. While this generates a nearly identical power curve, for the particular change in inductance, graphs (b) and (c) show the peak P_a over a broader range of α and β values; however, no significant changes occur in the peak P_a value.

Although the above results only affirm the findings from prior works and do not highlight the influence of retaining the inductance term in the analysis, the graphs of Fig. 9 focus on a case where the peak power is altered by the inductance. More specifically, the solid line of Fig. 9 a shows the same P_a curve as Fig. 8 a; however, multiplying α and β by a constant to mimic an inductance change, gives the dotted P_a curve—a distinctly different result. Fig. 9 a highlights the primary difference of including the inductance term in the analysis, i.e. the peak P_a is dependent upon both the resistive load and the inductance. This observation is further substantiated by the graphs (b) and (c) of Fig. 9 since the peak P_a value of graph (a) can substantially change for small changes in α and β. However, the maximum P_a value plateaus and becomes independent of α and β beyond some threshold. Fig. 10 provides additional insight into the behavior shown in Fig. 9. This figure shows that larger β values increase the rate of change in η_b due to solitary changes in α—at least for small values of α.

To summarize, we have shown that inductance changes can alter the average peak power for relatively small values of α and β. In addition, we have also shown that inductance changes have a negligible effect on P_a for sufficiently large values of α and β.

4.2. Periodic-excitation case

The ratio of the instantaneous power delivered to the electrical load to $\hat{P}_m$ is given by

$$P(\tau) = \frac{\hat{i}_m^2 I^2}{\hat{P}_m} R_L = \frac{R_L}{2R_i} \left(\sum_{p=1}^\infty b_p \cos p(\eta\tau + \psi) \right)^2.$$
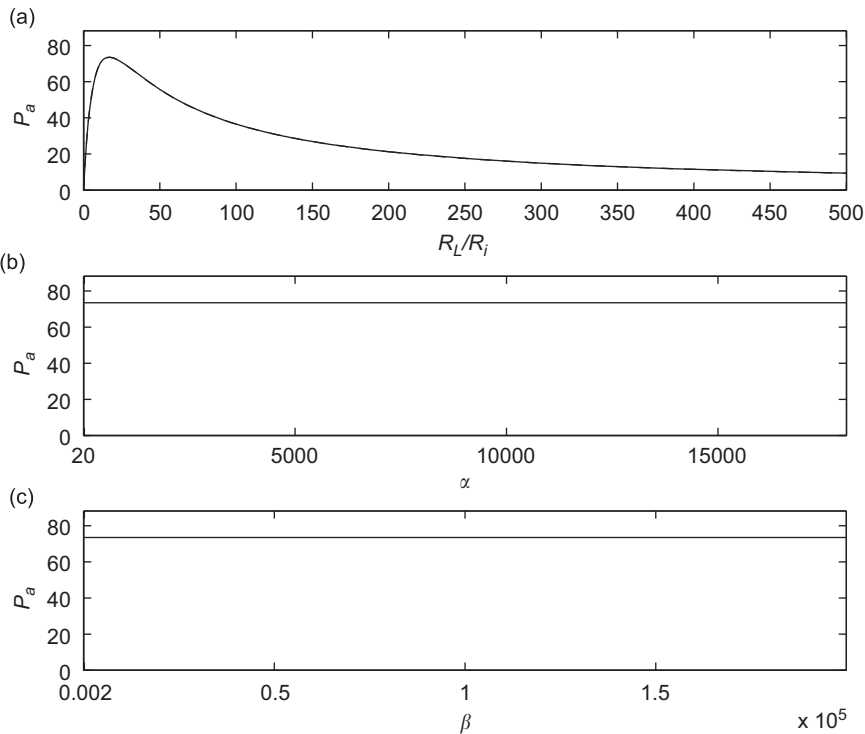
(32)

Fig. 8. Dimensionless average power curves plotted as a function of R_L/R_i (graph (a)). Solid line shows the P_a curve for $\beta = 2.0 \times 10^5$ and $1 \times 10^3 \leqslant \alpha \leqslant 501 \times 10^3$; the dotted line shows P_a for $\beta = 222$ and $1.1 \leqslant \alpha \leqslant 557$. Graphs (b) and (c) use a constant $R_L/R_i = 17$ value while varying the inductance to change α and β. The remaining parameters required to generate these graphs are $\zeta = 0.05$, $\gamma = 8 \times 10^{-3}$, $A = 1/20$, and $\eta = 1$.
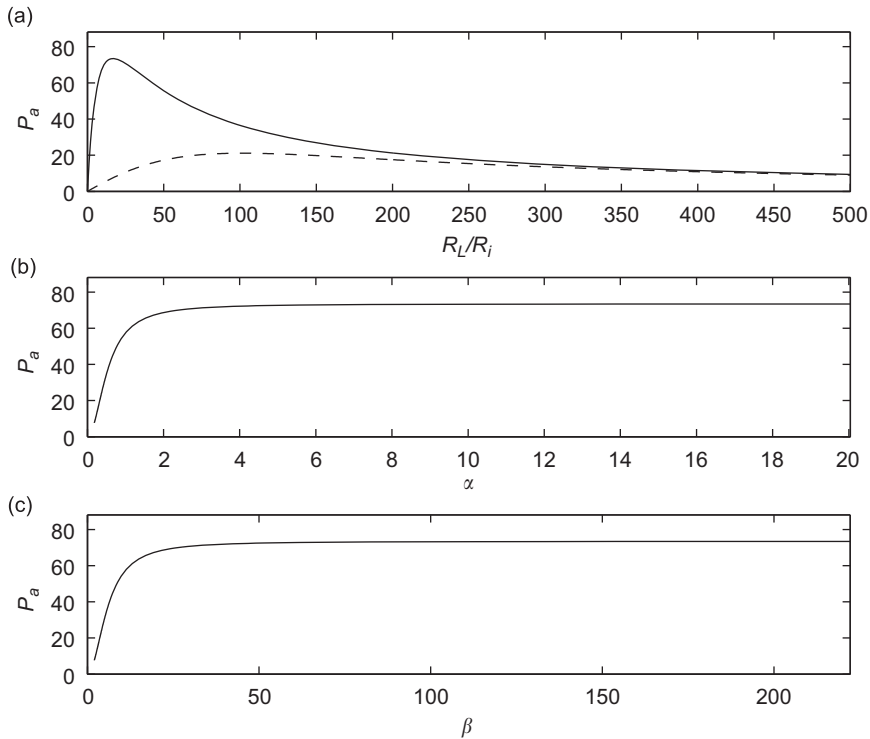
Fig. 9. Dimensionless average power curves plotted as a function of R_L/R_i (graph (a)). Solid line shows the P_a curve for $\beta = 222$ and $1.1 \leqslant \alpha \leqslant 557$; the dotted line shows P_a for $\beta = 2$ and $0.01 \leqslant \alpha \leqslant 5$. Graphs (b) and (c) use a constant $R_L/R_i = 17$ value while varying the inductance to change α and β. The remaining parameters required to generate these graphs are $\zeta = 0.05$, $\gamma = 8 \times 10^{-3}$, $A = \frac{1}{20}$, and $\eta = 1$.
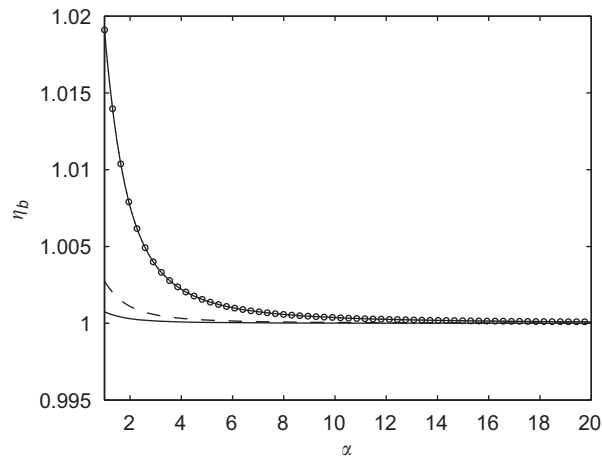

Fig. 10. Dimensionless resonance frequency plotted as a function of α. Each curve represents the following value of β: solid line $\beta = 1$, dashed line $\beta = 2$, and solid line with ∘ markers for $\beta = 10$. The following additional parameters were used: $\zeta = 0.05$ and $\gamma = 8 \times 10^{-3}$.

Although the above series is written for an infinite number of terms, reasonably accurate results are typically obtained with a truncated series expansion. The ratio of the average power to $\hat{P}_m$ is obtained by integrating Eq. (32) over a single period,

$$P_a = \frac{1}{T} \int_0^T P(\tau) \, \mathrm{d}\tau = \frac{R_L}{2R_i} \sum_{p=1}^{\infty} b_p^2, \tag{33}$$

where $T = 2\pi/\eta$ still holds. It is interesting to note that the expression for P_a simplifies due to the orthogonality in the response harmonics.
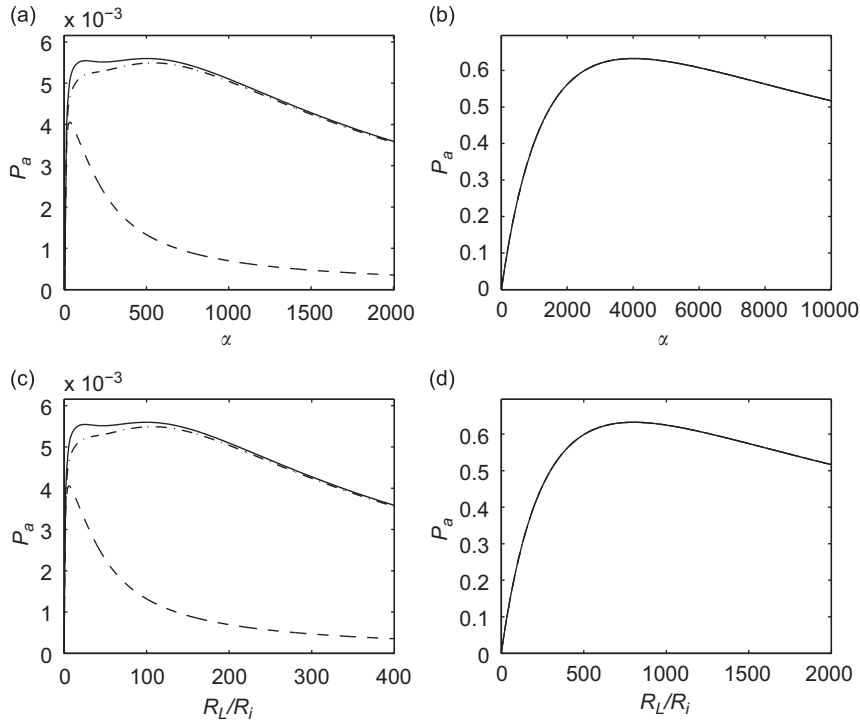
Fig. 11. Dimensionless average power plotted as a function of α and R_L/R_i for the approximated excitation of Fig. 6. Graphs (a) and (c) are for $\eta = 0.15$ and graphs (b) and (d) show results at resonance, $\eta = 1$. The number of harmonics used to determine P_a is denoted as follows: 5 harmonics (dashed line), 20 harmonics (dashed-dot line), and 50 harmonics (solid line). The following parameters were used to generate these graphs $\beta = 100$, $\zeta = 0.01$, and $\gamma = 0.8$.

Fig. 11 shows P_a predictions for the approximated square wave examined in Fig. 6. The fact that the P_a curve contained multiple local maxima was an interesting outcome for the $\eta = 0.15$ case. In addition, this case required a relatively larger number of harmonics, in comparison to the $\eta = 1$ case of the second column, before the predictions converged. For instance, the P_a predictions for the $\eta = 1$ case showed convergence when less than 5 harmonics were used, but the predictions for the $\eta = 0.15$ case did not converge until more than 20 harmonics were applied.

4.3. Narrow-band noise case

The ratio of the instantaneous power delivered to the electrical load to $\hat{P}_m$ is given by

$$P(\tau) = \frac{i_m^2 I^2}{\hat{P}_m} R_L = \frac{R_L}{2R_i} \left(\sum_{r=1}^{\infty} b_r \cos(\eta_r \tau + \psi_r) \right)^2. \tag{34}$$

While the analytical expression for the ratio of the average power to $\hat{P}_m$ is given by

$$P_a = \frac{1}{T} \int_0^T P(\tau) \, d\tau = \frac{1}{2T} \frac{R_L}{R_i} \int_0^T \left(\sum_{r=1}^{\infty} b_r \cos(\eta_r \tau + \psi_r) \right)^2, \tag{35}$$

this expression cannot be reduced to a more convenient form since the harmonics of the response are not orthogonal over any single period. In addition, the time interval to use for the averaging also seems somewhat ambiguous since a primary harmonic does not exist. Despite these complications, we still believe P_a to be a beneficial metric for characterizing the power. To illustrate why this becomes a reasonable metric, Eq. (34) was plotted for two different frequency bands in Fig. 12. This was done by creating normally distributed random vectors for η_r and λ_r and then using the solutions from Eqs. (28b) and (29a) to solve for b_r and ψ_r, respectively. The two important observations from Fig. 12 and all of the other cases we investigated are: (1) more energy is harvested when the resonance lies within the frequency band of the excitation; and (2) $P(\tau)$ contains small oscillations about a mean value; thus P_a can be readily obtained from the mean of $P(\tau)$ or by using Eq. (35) and an integer number of periods for the lowest frequency.
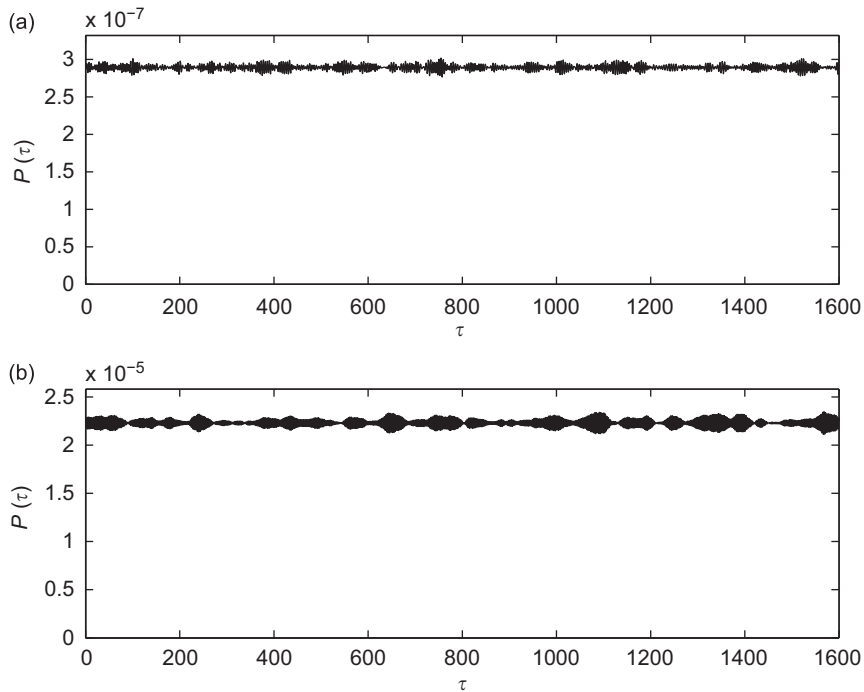
Fig. 12. Dimensionless power plotted as a function dimensionless time using 5×10^3 frequencies. Graph (a) shows results for $0.25 \leqslant \eta \leqslant 0.75$ and graph (b) shows results for $0.75 \leqslant \eta \leqslant 1.25$. The remaining parameters required to generate these graphs are $\zeta = 0.01$, $\alpha = 2500$, $\beta = 10$, $\gamma = 8$, and $\Gamma = 5 \times 10^{-3}$.

5. Conclusions

This paper obtains analytical solutions for the linear response behavior of an energy harvester that uses electromagnetic induction to convert ambient vibration into electrical energy. The model for an archetypal harvester was derived and investigated for the case of directly powering a resistive load. The mathematical model was non-dimensionalized and analytical solutions for the system's response were presented for three types of ambient excitations. The analytical solutions were then used to study the power delivered to an electrical load.

The present study does not assume the circuit inductance to be negligible; instead, we provide evidence that suggests the inductance can sometimes alter the optimum power transferred to an electrical load. In addition, the results of Fig. 4 show the peak current can occur at a frequency away from the natural frequency. Response and average power results indicate matching the device resonance to the primary harmonic of the periodic excitation will typically yield the best performance. However, our investigations for relatively small values of α and β, results that were not included, were found to display similar behavior to the single-frequency excitation case with peak power that can occur away from $\eta = 1$. Power studies for narrow-band white noise indicate that the average power can be used in comparative studies of device performance.

In summary, the primary novelty of the present study is the development of closed-form solutions for the harvester response to single-harmonic, periodic, and narrow-band white noise excitations. The presented solutions include the circuit inductance and highlight regions, in dimensionless parameter space, where the optimum power is altered by inductance. Finally, we expect the presented analytical solutions to impact the design choices for future energy harvesters for two reasons: (1) we have shown the maximum power transferred to an electrical load can be altered by the inductance; and (2) the inductance could potentially be used to tune the resonance to achieve peak power.

References

[1] T. von Buren, G. Troster, Design and optimization of a linear vibration-driven electromagnetic micro-power generator, *Sensors and Actuators A* 135 (2007) 765–775.

[2] B.P. Mann, N.D. Sims, Energy harvesting from the nonlinear oscillations of magnetic levitation, *Journal of Sound and Vibration* 319 (2009) 515–530.
[3] S. Roundy, P.K. Wright, J.M. Rabaey, *Energy Scavenging for Wireless Sensor Networks*, Springer, New York, 2003.
[4] B.C. Yen, J.H. Lang, A variable-capacitance vibration-to-electric energy harvester, *IEEE Transactions on Circuits and Systems 1—Fundamental Theory and Applications* 53 (2) (2005) 288–295.
[5] X. Zhao, D.G. Lord, Application of the villari effect to electrical power harvesting, *Journal of Applied Physics* 99 (08M703).
[6] J.M. Renno, M.F. Daqaq, D.J. Inman, On the optimal energy harvesting from a vibration source, *Journal of Sound and Vibration* 320 (2009) 386–405.
[7] S. Roundy, On the effectiveness of vibration based energy harvesting, *Journal of Intelligent Systems and Structures* 16 (2005) 809–823.
[8] S.M. Shahruz, Limits of performance of mechanical band-pass filters used in energy scavenging, *Journal of Sound and Vibration* 293 (1–2) (2006) 449–461.
[9] C.B. Williams, R.B. Yates, Analysis of a microgenerator for microsystems, *Proceedings of the 8th International Conference on Solid-State Sensors and Actuators*, Stockholm, Sweden, Eurosensors IX, 1995, pp. 87–B4.
[10] A. Triplett, D.D. Quinn, The effect of non-linear piezoelectric coupling on vibration-based energy harvesting, *Journal of Intelligent Material Systems and Structures* 20 (16) (2009) 1959–1967.
[11] S.C. Stanton, C. McGeehee, B.P. Mann, Reversible hysteresis for broadband magnetopiezoelastic energy harvesting, *Applied Physics Letters* 95 (174103) (2009) 1–3.
[12] B.P. Mann, B.A. Owens, Investigations of a nonlinear energy harvester with a bistable potential well, *Journal of Sound and Vibration*, in press, doi:10.1016/j.jsv.2009.11.034.
[13] I. Sari, T. Balkan, H. Kulah, An electromagnetic micro power generator for wideband environmental vibrations, *Sensors and Actuators A* 145–146 (2008) 405–413.
[14] S.M. Shahruz, Design of mechanical band-pass filters for energy scavenging, *Journal of Sound and Vibration* 292 (3–5) (2006) 987–998.
[15] E.S. Leland, P.K. Wright, Resonance tuning of piezoelectric vibration energy scavenging generators using compressive axial load, *Smart Material and Structures* 15 (2006) 1413–1420.
[16] N.G. Stephen, On energy harvesting from ambient vibration, *Journal of Sound and Vibration* 293 (2006) 409–425.
[17] B. Yang, C. Lee, W. Xiang, J. Xie, J.H. He, R.K. Kotlanka, S.P. Low, H. Feng, Electromagnetic energy harvesting from vibrations of multiple frequencies, *Journal of Micromechanics and Microengineering* 19 (035001) (2009) 1–8.
[18] S.P. Beeby, R.N. Torah, M.J. Tudor, P. Glynne-Jones, T. O'Donnell, C.R. Saha, S. Roy, A micro electromagnetic generator for vibration energy harvesting, *Journal of Micromechanics and Microengineering* 17 (2007) 1257–1265.
[19] C.R. Saha, Optimization of and electromagnetic energy harvesting device, *IEEE Transactions on Magnetics* 42 (10) (1942) 3509–3511.
[20] G. Poulin, E. Sarraute, F. Costa, Generation of electrical energy for portable devices comparative study of an electromagnetic and piezoelectric system, *Sensors and Actuators A* 116 (2004) 461–471.
[21] S. Kulkarni, E. Koukharenko, R. Torah, J. Tudor, Design, fabrication and test of integrated macro-scale vibration-based electromagnetic generator, *Sensors and Actuators A* 145–146 (2008) 336–342.
[22] P. Glynne-Jones, M.J. Tudor, S.P. Beeby, N.M. White, An electromagnetic, vibration-powered generator for intelligent sensor systems, *Sensors and Actuators A* 110 (2004) 344–349.
[23] S.P. Beeby, M.J. Tudor, N.M. White, Energy harvesting vibration sources for microsystems applications, *Measurement Science and Technology* 17 (2006) 175–195.
[24] Y. Jin, H. Hu, Dynamics of a Duffing oscillator with two time delays in feedback control under narrow-band random excitation, *Journal of Computation and Nonlinear Dynamics* 3 (2008) 1–7.